Magnetars as powering sources of gamma-ray burst associated supernovae, and unsupervized clustering of cosmic explosions

Amit Kumar [ORCID],[1]★ Kaushal Sharma [ORCID],[2] Jozsef Vinkó [ORCID],[3,4,5,6] Danny Steeghs [ORCID],[1] Benjamin Gompertz [ORCID],[7] Joseph Lyman [ORCID],[1] Raya Dastidar [ORCID],[8,9] Avinash Singh [ORCID],[10] Kendall Ackley [ORCID][1] and Miika Pursiainen [ORCID][1]

[1]*Department of Physics, University of Warwick, Gibbet Hill Road, Coventry CV4 7AL, UK*
[2]*Forensic Science Laboratory Uttar Pradesh, Moradabad - 244 001, India*
[3]*Konkoly Observatory, HUN-REN Research Center for Astronomy and Earth Sciences, Konkoly Thege M. ut 15-17, Budapest 1121, Hungary*
[4]*Department of Experimental Physics, University of Szeged, Dom ter 9, Szeged 6720, Hungary*
[5]*ELTE Eötvös Loránd University, Department of Physics and Astronomy, Pázmány Péter sétány 1/A, Budapest 1117, Hungary*
[6]*Department of Astronomy, University of Texas, Austin, TX 79712, USA*
[7]*Institute of Gravitational Wave Astronomy and School of Physics and Astronomy, University of Birmingham, Birmingham B15 2TT, UK*
[8]*Instituto de Astrofísica, Universidad Andres Bello, Fernandez Concha 700, Las Condes, Santiago RM, Chile*
[9]*Millennium Institute of Astrophysics, Nuncio Monsenor Sótero Sanz 100, Providencia, Santiago 8320000 Chile*
[10]*Hiroshima Astrophysical Science Centre, Hiroshima University, 1-3-1 Kagamiyama, Higashi-Hiroshima, Hiroshima 739-8526, Japan*

ABSTRACT

We present the semi-analytical light curve modelling of 13 supernovae associated with gamma-ray bursts (GRB-SNe) along with two relativistic broad-lined (Ic-BL) SNe without GRB association (SNe 2009bb and 2012ap), considering millisecond magnetars as central-engine-based power sources for these events. The bolometric light curves of all 15 SNe in our sample are well-regenerated utilizing a χ^2-minimization code, MINIM, and numerous parameters are constrained. The median values of ejecta mass ($M_{\rm ej}$), magnetar's initial spin period ($P_{\rm i}$), and magnetic field (B) for GRB-SNe are determined to be $\approx 5.2\,{\rm M_\odot}$, 20.5 ms, and 20.1 × 10^{14} G, respectively. We leverage machine learning (ML) algorithms to comprehensively compare the three-dimensional parameter space encompassing $M_{\rm ej}$, $P_{\rm i}$, and B for GRB-SNe determined herein to those of H-deficient superluminous SNe (SLSNe-I), fast blue optical transients (FBOTs), long GRBs (LGRBs), and short GRBs (SGRBs) obtained from the literature. The application of unsupervised ML clustering algorithms on the parameters $M_{\rm ej}$, $P_{\rm i}$, and B for GRB-SNe, SLSNe-I, and FBOTs yields a classification accuracy of ∼95 per cent. Extending these methods to classify GRB-SNe, SLSNe-I, LGRBs, and SGRBs based on $P_{\rm i}$ and B values results in an accuracy of ∼84 per cent. Our investigations show that GRB-SNe and relativistic Ic-BL SNe presented in this study occupy different parameter spaces for $M_{\rm ej}$, $P_{\rm i}$, and B than those of SLSNe-I, FBOTs, LGRBs, and SGRBs. This indicates that magnetars with different $P_{\rm i}$ and B can give birth to distinct types of transients.

Key words: methods: analytical – methods: statistical – techniques: photometric – stars: magnetars – gamma-ray bursts – transients: supernovae.

1 INTRODUCTION

Long gamma-ray bursts (LGRBs) with[1]$T_{90} \gtrsim 2$ s (Kouveliotou et al. 1993) are thought to emerge from the death of rapidly rotating, metal-poor, and massive stars (e.g. Wolf–Rayet; Woosley 1993; Woosley, Heger & Weaver 2002; Piran 2004; Zhang, Woosley & Heger 2004; Maeder & Meynet 2012; Zhang 2019). These stars have been stripped of their H/He-envelopes and are sporadically found associated with H/He-deficient broad-lined supernovae (Ic-BL SNe, known as GRB-SNe, Woosley & Bloom 2006; Li & Hjorth 2014; Modjaz et al.

2016; Cano et al. 2017b; Dainotti et al. 2022). On the other hand, short GRBs (SGRBs) with $T_{90} \lesssim 2$ s are theorized to originate from compact binary mergers (e.g. neutron star (NS)-NS, NS-black hole) and are sometimes found associated with kilonovae (Eichler et al. 1989; Tanaka 2016; Metzger 2019), e.g. GRB 170817A associated with a kilonova named AT 2017gfo and the gravitational-wave event GW 170 817 (Abbott et al. 2017a, b; Goldstein et al. 2017; Pian et al. 2017; Troja et al. 2017; Valenti et al. 2017; Wang et al. 2017b). This case serves as solid evidence favouring compact binary mergers as progenitors for SGRBs. Nevertheless, LGRBs like nearby GRB 211211A (at 350 Mpc, Rastinejad et al. 2022; Troja et al. 2022; Yang et al. 2022; Gompertz et al. 2023) and recently discovered GRB 230307A (second brightest LGRB, Dai et al. 2023; Gillanders et al. 2023; Levan et al. 2023; Sun et al. 2023) exhibited possible kilonovae association and compact binary merger systems as likely progenitors. Similarly, cases like GRB 200826A demonstrated the

★ E-mail: amitkundu515@gmail.com (AK); amit.kumar.3@warwick.ac.uk (AK)

[1]The time span during which 90 per cent of the entire background-subtracted counts are observed in the γ/X-ray bands.

converse, where a SN is associated with an SGRB originating from the collapse of a massive star (Ahumada et al. 2021; Zhang et al. 2021; Rossi et al. 2022). These cases challenge the previously established dichotomy between progenitor and underlying powering mechanism scenarios of LGRBs and SGRBs, prompting a reassessment of our understanding (see Gottlieb et al. 2023b). This also motivates further investigations into the LGRBs and SNe connections, where the presence of a SN can reliably diagnose the progenitor star.

The era of LGRBs and Ic-BL SNe connections started with the discovery of the first direct temporal and spatial connection of the closest GRB 980425 and SN 1998bw ($z = 0.00866$, Galama et al. 1998; Iwamoto et al. 1998; Wang & Wheeler 1998; Patat et al. 2001). The association of a SN with a GRB can be seen as a late-time bump in the optical/near-infrared (NIR) light curves after the fading of the afterglow (AG), nearly 2–3 d after the burst. Other signatures include the emerging broader absorption feature in the spectra and the blackbody component in the spectral energy distribution (Woosley & Bloom 2006; Ghirlanda et al. 2007; Kumar & Zhang 2015; Izzo et al. 2019). Over the last two decades, this field has evolved enormously, with more than fifty GRBs and SNe association events (Dainotti et al. 2022; Li et al. 2023), thirty of which have also been classified spectroscopically (Aimuratov et al. 2023). In addition, the one and only known case of superluminous (SL) SN 2011kl associated with an ultra-long (UL) GRB 111209A (Greiner et al. 2015; Gompertz & Fruchter 2017; Kann et al. 2019) devised further opportunities to explore whether H/He-deficient SLSNe (SLSNe-I) are also associated with LGRBs or if this was a particular case. Numerous studies suggest that GRB-SNe/LGRBs and SLSNe-I share similarities in their progenitors (Lunnan et al. 2015; Mösta et al. 2015; Levan et al. 2016; Aguilera-Dena et al. 2018) and host environments (Kelly, Kirshner & Pahre 2008; Lunnan et al. 2014; Angus et al. 2016) to some extent. Another probable contributing factor to these events' diversity in observed properties could be the underlying powering mechanism, influencing how stars end their lives differently. The collapse of massive stars, which could be the origin of GRB-SNe/LGRBs and SLSNe-I, might result in the formation of centrally-located millisecond magnetars (or mass-accreting black holes, Woosley 1993; Popham, Woosley & Fryer 1999; Narayan, Piran & Kumar 2001). Therefore, magnetars could be potential central-engine-based power sources for these events (Usov 1992; Thompson 1994; Dai & Lu 1998; Zhang & Mészáros 2001; Woosley 2010; Metzger et al. 2011; Hu et al. 2023).

The centrally-located new-born millisecond magnetar induces relativistic Poynting flux or magnetically driven baryonic bipolar jets that bore through the stellar envelope and lead to GRB formation far from its progenitor (Duncan & Thompson 1992; Usov 1992; Bucciantini et al. 2008). The collision of faster-moving shells with slower ones within the jet generates internal shocks, producing a primary γ-ray burst (prompt emission), while jet-ambient medium interaction leads to the formation of AG, visible across the electromagnetic spectrum; the standard fireball model (Meszaros & Rees 1993; Piran 1999; Fox & Mészáros 2006). Through magnetic braking, the strong magnetic field of the magnetar can dissipate its rotational energy into the jet and lead to a distinctive bump in the GRB light curve, observed as a X-ray plateau (Dai et al. 2006; Rowlinson et al. 2013). Additionally, this magnetic braking effect or jet-ejecta interaction can also thermalize expanding ejecta, raise its temperature, and power the associated SN (Kasen & Bildsten 2010; Woosley 2010; Dessart et al. 2012; Sobacchi et al. 2017; Barnes et al. 2018; Burrows & Vartanyan 2021). A magnetar with a mass of $1.4\,M_{\odot}$, a spin period of 1 ms and a 10 km radius holds a rotational energy reservoir of $\sim 2 \times 10^{52}$ erg (Duncan & Thompson 1992; Usov 1992), which

is sufficient for driving a GRB and energizing the accompanying SN (Mazzali et al. 2014). With the capability of holding such a high energy reservoir, magnetars as central-engine-based powering sources can govern various types of transients, from extreme SNe to GRBs (Usov 1992; Wheeler et al. 2000; Woosley 2010; Metzger et al. 2015; Kashiyama et al. 2016; Margalit et al. 2018; Inserra 2019; Shankar et al. 2021; Ho et al. 2023; Omand & Sarin 2024).

The presence of an internal plateau, characterized by a plateau followed by an immensely sharp decay in the X-ray light curves (exhibited by ~80 per cent of LGRBs and around 50 per cent of SGRBs, Troja et al. 2007; Lyons et al. 2010; Rowlinson et al. 2010, 2013, 2014; Yi et al. 2014; Lü et al. 2015; Zou et al. 2019; Suvorov & Kokkotas 2021; Zou et al. 2021), extended emission in SGRBs (Gompertz et al. 2013; Gompertz, O'Brien & Wynn 2014; Gompertz et al. 2015; Gibson et al. 2017), precursor (Burlon et al. 2008; Troja, Rosswog & Gehrels 2010), and flaring activities (Dall'Osso et al. 2017; Gibson et al. 2018; Saji, Iyyani & Mazde 2023) in GRBs support the underlying magnetars as power sources (see also Bernardini 2015). On the other hand, magnetars have also been suggested as the power sources to explain the properties of different SNe types, including SLSNe-I (Quimby et al. 2011; Inserra et al. 2013; Nicholl et al. 2017; Yu et al. 2017; Dessart 2019; Kumar et al. 2021b), GRB-SNe (Mazzali et al. 2014; Cano, Johansson Andreas & Maeda 2016; Wang et al. 2017a; Barnes et al. 2018; Lü et al. 2018; Kumar et al. 2021a, 2022; Lian et al. 2022), Ic-BL SNe without GRB association (classical Ic-BL SNe, e.g. SN 1997ef and SN 2007ru, Wang et al. 2016), Ic (PTF SN 2019cad; Gutiérrez et al. 2021), Ib (SN 2005bf, Maeda et al. 2007 and SN 2012u, Pandey et al. 2021; Omand & Jerkstrand 2023), and also fast blue optical transients (FBOTs, Hotokezaka, Kashiyama & Murase 2017; Prentice et al. 2018; Fang et al. 2019; Liu et al. 2022). In this paper, we follow the notation FBOT, which refers to all fast-evolving transients (as presented in, e.g. Drout et al. 2014; Pursiainen et al. 2018). Different magnetar properties, such as the initial spin period (P_i), magnetic field (B), and the central engine activity duration, can give rise to different types of transients, e.g. a faster-rotating magnetar leads to a more energetic GRB (Zou et al. 2019, 2021). Hence, investigating the characteristics of the central engine powering sources and comparing them across various types of transients can provide valuable insights into the distinct properties of these transients.

Numerous studies have probed the underlying powering mechanisms of GRB-SNe; however, most of these are primarily centred around single-event analyses. Several of these studies also suggested a millisecond magnetar as a powering source, such as Soderberg et al. (2006), Margutti et al. (2013), Greiner et al. (2015), and Barnes et al. (2018). Some of the previous studies also attempted light curve modelling on a limited sample of GRB-SNe (e.g. Cano et al. 2016; Kumar et al. 2022; Lian et al. 2022). Cano et al. (2016) conducted modelling on seven LGRBs and their associated SNe, considering magnetars as power sources for these events. However, for all cases except GRB 111209A/SN 2011kl, their model could fit the AG part but not the SN part; hence, they suggested ^{56}Ni-decay as an additional power source. Lian et al. (2022) explained the light curves of three GRBs and their associated SNe using a hybrid model containing power law + ^{56}Ni-decay. Kumar et al. (2022) also performed the light curve modelling of three GRB-SNe using ^{56}Ni-decay, spin-down millisecond magnetar (MAG), circumstellar matter interaction (CSMI), and CSMI + ^{56}Ni-decay models and found that the MAG is the only model that adequately explained the light curves of all three GRB-SNe. Additionally, Barnes et al. (2018) conducted spectral and light curve modelling of GRB-SNe through

2D relativistic hydrodynamics and radiation transport calculations, considering a magnetar solely as a powering source, without adding any additional power source. The yielded synthetic spectra and light curves align seamlessly with observed GRB-SNe.

The present work focuses on the MAG model-based light curve modelling of all the GRB-SNe in the literature with good data coverage. Based on the findings of Barnes et al. 2018 and Kumar et al. 2022, the current work operates under the assumption that a millisecond magnetar is the primary power source for GRB-SNe. It is crucial, however, to acknowledge that contributions from the ^{56}Ni-decay and CSMI can still play a role in at least some of these events. However, this assumption allows us to perform light curve modelling on GRB-SNe using a singular approach and examine, where the underlying magnetar's parameters align in comparison to other previously asserted magnetar-powered cosmic transients, e.g. SLSNe-I, FBOTs, LGRBs, and SGRBs. We also leverage unsupervized machine learning (ML) algorithms to understand these distinctions. The prominence of ML algorithms in astronomy is evident in their application for both supervized and unsupervized classification tasks (Boone 2019; Chatzopoulos & Tuminello 2019; Villar et al. 2020; Sharma et al. 2020a, b; Chen et al. 2023; Dimple, Misra & Arun 2023; Kisley et al. 2023; de Soto et al. 2024). Our approach involves the implementation of *k*-means clustering, among other clustering algorithms, to differentiate between various transient phenomena based on their positions in the parameter space.

The paper is organized as follows. In Section 2, we elaborate on the criteria employed for sample selection and provide details regarding the estimation/collection of bolometric light curves. The light-curve modelling is presented in Section 3. Section 4 comprehensively discusses the obtained results. Finally, the findings are concluded in Section 5.

2 SAMPLE SELECTION AND DATA COLLECTION

The optical/NIR light curves of a typical GRB accompanying a SN show power-law decay in the initial phases, followed by late-time rebrightening. This rebrightening consists of contributions from the AG of the GRB, the underlying SN, and the constant flux from the host galaxy (Woosley & Bloom 2006; Cano et al. 2017b; Klose et al. 2019). Extracting contributions from each phenomenon is straightforward. Either template subtraction or subtracting a constant flux can be used to remove the host galaxy contribution. Fitting a single or a set of broken power laws to the early phases light curve ($\lesssim 2$ d), extrapolating it up to the late phase, and subtracting from the AG + SN light curve can be used to get the separated light curves for AG and SN (see Cano et al. 2017b for details). A great deal of physical information can be manifested by individually modelling the three components (AG, SN, and host). The present work focuses on the semi-analytical bolometric light-curve modelling of all the GRB-SNe (SN part only, after removing AG and host contributions, as discussed in Kumar et al. 2022) in the literature with adequate data coverage.

The initial task involves collecting/estimating the multiband/bolometric light curves of GRB-SNe. The selection criteria for the GRB-SNe sample in this study are primarily based on three considerations: 1) ensuring the number of data points in each filter exceeds the free parameters of the model employed (i.e. six in our case), 2) requiring data availability in at least three optical filters to generate the bolometric light curve with appropriate wavelength coverage, and 3) necessitating data around the peak to enhance the constraints on model parameters. Cano et al. (2017b) conducted a

statistical study on GRB-SNe reported until 2015, generated their bolometric light curves, and discussed their physical properties. Among all the GRB-SNe discussed by Cano et al. (2017b) and references therein, we selected nine events (SNe 1998bw, 2003dh, 2003lw, 2006aj, 2010bh, 2010ma, 2011kl, 2012bz, and 2013dx) based on the criteria mentioned above. We further enriched our sample with GRB-SNe discovered after 2015, following the criteria mentioned above: SN 2016jca (Cano et al. 2017a; Ashall et al. 2019), SN 2017htp (de Ugarte Postigo et al. 2017; Melandri et al. 2019; Kumar et al. 2022), SN 2017iuk (Wang et al. 2018; Izzo et al. 2019; Suzuki, Maeda & Shigeyama 2019; Kumar et al. 2022), and SN 2019jrj (Melandri et al. 2022). Some GRB-SNe are excluded from the sample because of larger uncertainties associated with their light curves during the SN phase, e.g. SN 2013cq (Melandri et al. 2014; Becerra et al. 2017), iPTF14bfu (Cano et al. 2015), SN 2022xiw (Fulton et al. 2023).

Furthermore, we have included two Ic-BL SNe 2009bb and 2012ap in our sample from Cano et al. (2017b, and references therein). Despite the absence of direct observational evidence linking these events to GRBs, their bright radio emissions suggest highly relativistic ejecta compared to normal Ib/c SNe, akin to subenergetic GRBs (e.g. GRB 980425, associated with SN 1998bw, see figs 2 and 3 of Margutti et al. 2014); see also Levesque et al. (2010); Pignata et al. (2011); Liu et al. (2015); Milisavljevic et al. (2015). Notably, these events with fainter *X*-ray emissions at late times exhibit no signs of late-time central engine activity, indicating them as among the weakest central engine-driven SNe, where jets hardly break out. This could be attributed to either a shorter-lived engine or a more extended stellar envelope (Bietenholz et al. 2010; Margutti et al. 2014; Chakraborti et al. 2015). Hence, it is interesting to explore the possibility of explaining these relativistic Ic-BL SNe using the MAG model employed in the present study and compare them with GRB-SNe.

Generating a robust bolometric light curve depends significantly on the wavelength coverage of the multiband data and the quality of the individual band data. Unfortunately, such high-quality data is uncommon and is available for only a handful of GRB-SNe. Simply assuming blackbody spectral energy distribution can result in large fitting uncertainties, especially with limited wavelength coverage. Therefore, in this study, we use quasi-bolometric light curves for light curve modelling, following a similar approach to Cano et al. (2017b), who used quasi-bolometric light curves to estimate various explosion parameters of GRB-SNe. The quasi-bolometric light curves of SNe 1998bw, 2003dh, 2003lw, 2006aj, 2009bb, 2010bh, 2010ma, 2011kl, 2012ap, 2012bz, and 2013dx are directly adopted from Cano et al. (2017b) and references therein. For SNe 2016jca, 2017htp, 2017iuk, and 2019jrj, quasi-bolometric light curves were independently estimated using the Superbol code (Nicholl 2018), following the procedure described in Kumar et al. (2020, 2021b). For consistency, the quasi-bolometric light curves are estimated by choosing $H_0 = 67.3 \, \text{km s}^{-1} \, \text{Mpc}^{-1}$, $\Omega_m = 0.315$, and $\Omega_m = 0.685$, as adopted by Cano et al. (2017b). The foreground Milky Way extinctions were corrected using dust maps by Schlafly & Finkbeiner (2011). The quasi-bolometric light curves of SNe 2016jca, 2017htp, 2017iuk, and 2019jrj are also compared to those presented in the literature (Cano et al. 2017a; Izzo et al. 2019; Kumar et al. 2022; Melandri et al. 2022), and they were found to be consistent. The quasi-bolometric light curves of all 15 SNe used in this study, along with their low-order spline fits, are shown in Fig. 1. The SNe presented in this study exhibit a wide range of peak quasi-bolometric luminosities (from ≈ 3 to 36×10^{42} erg s^{-1}), with SN 2011kl showing the highest peak luminosity and relativistic Ic-BL SNe 2009bb and
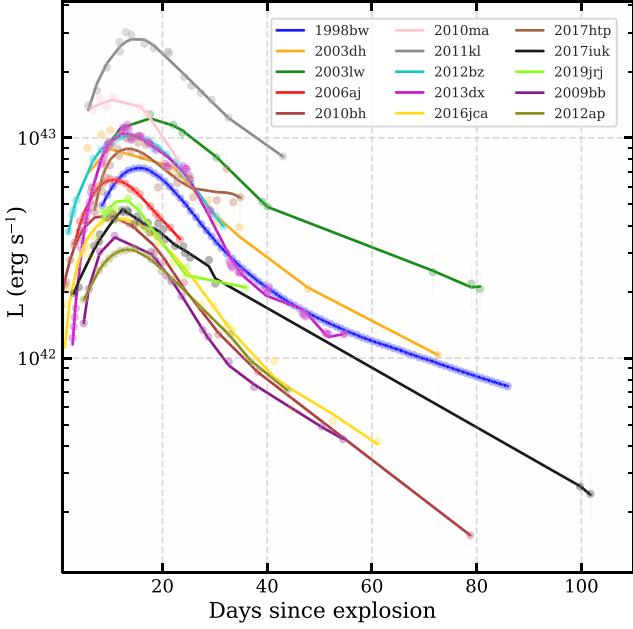
Figure 1. The quasi-bolometric light curves of the 13 GRB-SNe and two relativistic Ic-BL SNe used in the present study, along with their low-order spline function fitting curves, are shown. Data courtesy: Cano et al. 2017a, b; Izzo et al. 2019; Melandri et al. 2019; Kumar et al. 2022; Melandri et al. 2022, and references therein.

2012ap displaying the lowest peak luminosities. Detailed discussions on the light curve properties of GRB-SNe are presented in Cano et al. (2017b).

3 LIGHT-CURVE MODELLING

This section delves into the semi-analytical light curve modelling of 13 GRB-SNe and two relativistic Ic-BL SNe used in the present study utilizing the MINIM code to investigate the spin-down magnetars as their possible powering sources. MINIM is a χ^2-minimization code designed in C++, suitable for semi-analytical light curve model fitting for SNe (Chatzopoulos et al. 2013). The code uses the Price's algorithm (Brachetti 1997), a random-search (direct-search or derivative-free) approach that effectively solves global optimization problems. At the same time, the code uses the Levenberg–Marquardt algorithm to obtain the final fine-tuned or best-fit model parameters. The common assumptions used by the MINIM code are the central location of the input power source, expansion of the SN-ejecta homologously, and dominant radiation pressure and separability of the spatial and temporal behaviour. Details about the MINIM code and its working strategy are elaborated in Chatzopoulos et al. (2013). Under the MAG model, the energy input from the centrally-located millisecond magnetar is determined by the dipole spin-down formula (Ostriker & Gunn 1971; Arnett & Fu 1989; Kasen & Bildsten 2010; Woosley 2010), which can be expressed in the form of the output luminosity from the photosphere of the SN ejecta as follows (adapted from Chatzopoulos, Wheeler & Vinko 2012; Chatzopoulos et al. 2013):

$$L(t) = 2Ae^{-[x_1^2 + rx_1]} \int_0^{x_1} e^{[x_1'^2 + rx_1']} \frac{x_1' + r}{(1 + x_2 x_1')^2} \, dx_1', \qquad (1)$$

Here, $A = \frac{E_p}{t_p}$ (E_p and t_p are the initial rotational energy and spin-down time-scale of the magnetar, respectively), $x_1 = \frac{t}{t_d}$, $x_2 = \frac{t_d}{t_p}$ (t,

t_d, and t_p are initial epoch since the burst, diffusion and characteristic time-scales, respectively), and $r = \frac{R_p}{(V_{exp} t_d)}$ is the ratio between the hydrodynamical and light-curve time-scales, where R_p is the progenitor radius and V_{exp} is the ejecta expansion velocity. The integration constant β is chosen as equal to 13.8. In all, there are six fitting parameters for the light-curve fitting using the MAG model: t, R_p, E_p, t_d, t_p, and V_{exp}. However, initial spin period and magnetic field are calculated as follows: $P_i = \left(\frac{2 \times 10^{50}\,\mathrm{erg\,s^{-1}}}{E_p}\right)^{0.5} \times 10\,\mathrm{ms}$ and $B = \left(\frac{1.3 \times P_{i0}^2}{t_{p,yr}}\right)^{0.5} \times 10^{14}\,\mathrm{G}$, as affirmed by Chatzopoulos et al. (2013). On the other hand, the expression for ejecta mass is derived as $M_{ej} \sim \frac{1}{2} \frac{\beta c}{\kappa} V_{exp} t_d^2$, which is adapted from Wheeler, Johnson & Clocchiatti (2015).[2] We would like to caution here that some of these parameters are degenerate and correlated with each other, as discussed extensively by Chatzopoulos et al. (2013). This parameter degeneracy may introduce bias in the uniqueness of the inferred fitting parameters. However, fitting provided by the MINIM code considers the effect of these parameter correlations and degeneracy while determining the fitting parameters and associated uncertainties, which makes our fits reliable; see Chatzopoulos et al. (2013) for details.

In the literature, for stripped-envelope SNe, diverse studies have adopted different electron-scattering opacity (κ) values ranging from ~ 0.01 to $0.2\,\mathrm{cm^2\,g^{-1}}$ for half to fully-ionized gas, respectively (Inserra et al. 2013). In the present study, we choose a constant $\kappa = 0.1\,\mathrm{cm^2\,g^{-1}}$, comparable to the value chosen by Arnett 1982, ($\kappa = 0.08\,\mathrm{cm^2\,g^{-1}}$), as also suggested by Inserra et al. (2013); Wheeler et al. (2015); Wang et al. (2017a). However, assuming κ as a constant value may not be the most accurate approach because it varies both in time and within the ejecta (Nagy 2018). None the less, using a more realistic κ, which accounts for the temporal and spatial dependence, would require complicated model calculations which are beyond the scope of this paper.

The quasi-bolometric light curves of all 15 events in our sample are well regenerated by the MAG model with low χ^2 per degree of freedom (dof) values. The best-fitted model light curves for all cases are shown in Fig. A1, and the best-fit parameters are tabulated in Table 1. For certain events with more significant uncertainties in their pseudo-bolometric light curves, the estimated χ^2/dof is less than one, potentially due to overestimation of error variance. Also, the light curves of some events (e.g. SN 2003dh) are poorly fitted because of the limited number of data points and larger error bars, resulting in higher uncertainties in the fitting parameters.

The estimated M_{ej} and V_{exp} values for our sample of GRB-SNe and relativistic Ic-BL SNe are consistent within error bars, with the exception of SN 2010ma in terms of M_{ej} values, when compared to the values obtained in previous studies, mostly estimated through spectral investigations (see Fig. A2). Before the comparison, the M_{ej} values were scaled to a similar κ value ($0.1\,\mathrm{cm^2\,g^{-1}}$), wherever feasible. The offset in the M_{ej} value for SN 2010ma, derived in the current study and obtained from existing literature, may arise from the use of different models.

Light curve modelling of the 13 GRB-SNe presented in this study exhibit median values of $E_p \approx 4.8 \times 10^{49}\,\mathrm{erg}$, $t_d \approx 17\,\mathrm{d}$, $t_p \approx 5.4\,\mathrm{d}$, $R_p \approx 7.2 \times 10^{13}\,\mathrm{cm}$, $V_{exp} \approx 24\,000\,\mathrm{km\,s^{-1}}$, $M_{ej} \approx 5.2\,\mathrm{M_\odot}$, $P_i \approx$

---

[2]We refrained from using the M_{ej} expression quoted in Chatzopoulos et al. (2013) due to a reported typo in the M_{ej} equation as initially presented in Arnett (1982), which persisted in subsequent works such as Chatzopoulos et al. (2012), Chatzopoulos et al. (2013), acknowledged by Wheeler et al. (2015).

Table 1. Optimal parameters obtained through light curve modelling under the MAG model for 13 GRB-SNe and two relativistic central-engine-driven Ic-BL SNe presented in this study. The median values for the GRB-SNe are also quoted. The tabulated parameters are estimated considering $\kappa = 0.1\,\mathrm{cm^2\,g^{-1}}$.

SN	E_p^a $(10^{49}\,\mathrm{erg})$	t_d^b (d)	t_p^c (d)	R_p^d $(10^{13}\,\mathrm{cm})$	V_{exp}^e $(10^3\,\mathrm{km\,s^{-1}})$	M_{ej}^f $(M_\odot)$	P_i^g (ms)	B^h $(10^{14}\,\mathrm{G})$	χ^2/dof
1998bw	2.67 (0.01)	12.35 (0.07)	9.49 (0.09)	19.26 (0.57)	30.81 (1.43)	3.62 (0.21)	27.38 (0.04)	19.38 (0.09)	1.06
2003dh	4.76 (0.60)	16.32 (2.01)	9.44 (1.49)	11.41 (2.35)	22.21 (8.57)	4.55 (2.88)	20.50 (1.30)	14.56 (1.15)	0.26
2003lw	3.62 (0.19)	19.77 (0.79)	4.90 (0.21)	84.67 (6.75)	20.59 (1.76)	6.20 (1.02)	23.51 (0.62)	23.17 (0.49)	1.05
2006aj	10.54 (0.72)	18.12 (1.21)	0.52 (0.05)	0.01 (0.36)	20.47 (6.39)	5.18 (2.31)	13.78 (0.47)	41.58 (2.18)	1.34
2010bh	2.89 (0.03)	15.79 (0.80)	3.69 (0.10)	0.04 (0.13)	29.54 (2.97)	5.67 (1.15)	26.32 (0.16)	29.87 (0.41)	1.58
2010ma	17.75 (1.96)	18.41 (0.51)	0.48 (0.19)	7.16 (1.02)	15.32 (3.67)	4.00 (1.18)	10.61 (0.59)	33.23 (6.65)	0.80
2011kl	11.87 (0.71)	12.68 (0.32)	12.70 (1.22)	10.26 (3.56)	24.46 (2.46)	3.03 (0.46)	12.98 (0.39)	7.95 (0.38)	1.21
2012bz	7.30 (0.22)	19.15 (0.13)	3.59 (0.14)	8.44 (1.18)	28.87 (4.72)	8.15 (1.44)	16.56 (0.25)	19.06 (0.38)	1.40
2013dx	4.36 (0.05)	13.65 (0.04)	5.38 (0.04)	10.62 (1.67)	23.52 (4.88)	3.37 (0.72)	21.42 (0.11)	20.13 (0.08)	2.66
2016jca	2.34 (0.08)	14.96 (0.57)	7.37 (0.82)	1.86 (0.50)	33.89 (3.91)	5.84 (1.12)	29.25 (0.51)	23.50 (1.31)	1.32
2017htp	5.43 (0.01)	17.15 (0.33)	13.94 (1.50)	0.07 (0.03)	14.37 (0.66)	3.25 (0.27)	19.18 (0.20)	11.21 (0.61)	0.57
2017iuk	2.64 (0.01)	17.01 (1.26)	10.91 (0.41)	0.05 (0.02)	28.72 (4.08)	6.40 (1.86)	27.50 (0.05)	18.16 (0.34)	1.74
2019jrj	6.14 (0.28)	19.51 (1.88)	1.09 (0.02)	0.51 (0.07)	23.93 (3.71)	7.01 (2.44)	18.04 (0.41)	37.75 (0.29)	0.98
Median	4.76 (0.07)	17.01 (0.20)	5.38 (0.07)	7.16 (0.20)	23.93 (1.29)	5.18 (0.40)	20.50 (0.14)	20.13 (0.12)	
Relativistic Ic-BL SNe									
2009bb	1.06 (0.01)	12.16 (0.15)	4.19 (0.04)	20.40 (7.55)	17.98 (6.80)	2.05 (0.82)	43.36 (0.28)	46.22 (0.19)	1.14
2012ap	1.20 (0.01)	16.17 (1.07)	6.71 (0.21)	29.63 (4.35)	21.38 (4.56)	4.30 (1.49)	40.77 (0.97)	34.34 (0.54)	1.26

Note. $^a E_p$: initial rotational energy in 10^{49} erg. $^b t_d$: diffusion time-scale in days. $^c t_p$: spin-down time-scale in days. $^d R_p$: radius of the progenitor star in 10^{13} cm. $^e V_{exp}$: ejecta expansion velocity in $10^3\,\mathrm{km\,s^{-1}}$. $^f M_{ej}$: ejecta mass in $M_\odot$. $^g P_i$: initial spin period in ms. $^h B$: magnetic field in 10^{14} G.

20.5 ms, and $B \approx 20.1 \times 10^{14}$ G. SN 2011kl, the brightest among all GRB-SNe discovered to date (see Fig. 1), shows the highest t_p (except for SN 2017htp) and E_p (except for SN 2010ma) and the lowest B values among all the cases discussed here. Whereas, SN 2010ma, the second most luminous GRB-SN in the sample, exhibits the highest E_p (and consequently lowest P_i) and lowest t_p values compared to all 15 events presented in Table 1. On the other hand, the two relativistic Ic-BL SNe 2009bb and 2012ap share the lowest E_p (or highest P_i) and highest B values (except for SN 2006aj) than those of GRB-SNe used in this study (see Table 1). The implications of these parameters are discussed in the following section.

4 RESULTS AND DISCUSSION

4.1 Ejecta mass versus initial spin period and magnetic field

We conducted a comprehensive analysis, comparing the P_i, B, and M_{ej} estimated through the light curve modelling employing the MAG model for GRB-SNe and relativistic Ic-BL SNe 2009bb and 2012ap presented in the current study with analogous parameters for SLSNe-I and FBOTs. The left-hand and the right-hand panels of Fig. 2, respectively, present P_i versus M_{ej} and B versus M_{ej} for 13 GRB-SNe (in green squares) and two relativistic Ic-BL SNe (in green squares with black boundary) calculated in the present study along with those of SLSNe-I (in orange circles; taken from Yu et al. 2017; Kumar et al. 2021b and references therein) and FBOTs (in blue pentagons) adopted from Liu et al. 2022 who analysed well-observed literature events such as AT 2018cow (e.g. Prentice et al. 2018; Perley et al. 2019), but also unclassified fast transients found in archival searches (e.g. Drout et al. 2014; Pursiainen et al. 2018).

This analysis highlights that GRB-SNe and two relativistic Ic-BL SNe studied here share different regions in the P_i versus M_{ej} and B versus M_{ej} parameter spaces than those of SLSNe-I and FBOTs (see the left-hand and right-hand panels of Fig. 2, respectively). We emphasize that the M_{ej} values for all events in our sample are calculated using $\kappa = 0.1\,\mathrm{cm^2\,g^{-1}}$, as detailed in Section 3. However, even considering a range of κ from 0.01 to $0.2\,\mathrm{cm^2\,g^{-1}}$, the widest

plausible spectrum of M_{ej} values for SNe in our sample spans $\sim$1 to $82\,M_\odot$, notably surpassing the M_{ej} range of FBOTs ($\sim$0.01 to $1\,M_\odot$; Liu et al. 2022). Furthermore, the M_{ej} range of GRB-SNe and relativistic Ic-BL SNe discussed herein does not encroach upon the overlapping region with SLSNe-I in the P_i versus M_{ej} and B versus M_{ej} parameter spaces. This is due to SNe in our sample exhibiting higher P_i and B values compared to those of SLSNe-I (see Fig. 2). In all, even when considering M_{ej} values across a κ range of 0.01 to $0.2\,\mathrm{cm^2\,g^{-1}}$, it becomes apparent that GRB-SNe and the two relativistic Ic-BL SNe 2009bb and 2012ap in our sample occupy a distinctive parameter space distinct from that of FBOTs and SLSNe-I.

Liu et al. (2022) also compiled the P_i versus M_{ej} for FBOTs, SLSNe-I, classical Ic-BL SNe, and GRB-SNe and claimed a universal correlation between P_i and M_{ej} as $P_i \propto M_{ej}^{-0.41}$, shown with the grey-dashed line in the left-hand panel of Fig. 2. However, while SLSNe-I and FBOTs appear to follow the relation in general, the GRB-SNe and relativistic Ic-BL SNe studied here do not seem to align with the suggested correlation. In the present study, the P_i values estimated for GRB-SNe and relativistic Ic-BL SNe in our sample are higher than those shown by Liu et al. 2022. The P_i values for these cases used by Liu et al. (2022) were not estimated via performing light curve modelling but calculated from the kinetic energy through the rotational energy of the magnetar based on the assumptions of the initial value of the kinetic energy $\lesssim 10^{50}$ erg, which could be the possible reason behind this discrepancy.

It is also worth noting that, in Fig. 2, GRB-SNe seem to have tighter clustering than FBOTs and SLSNe-I, which is primarily attributed to the comparatively narrower range of peak luminosities (from $\sim$3 to $36 \times 10^{42}\,\mathrm{erg\,s^{-1}}$) in our GRB-SNe sample and the utilization of a fitting procedure with only six free parameters. On the other hand, the broad range of peak luminosities (from $\sim$2.9 $\times$ 10^{41} to $5.4 \times 10^{45}\,\mathrm{erg\,s^{-1}}$) and wider evolution time-scales of FBOTs' sample used by Liu et al. (2022) possibly contributed to scattered fitting parameters, which could also heightened by their employment of light-curve fitting model with eight free parameters compared to six in the present study. Similarly, for SLSNe-I, a broad range of
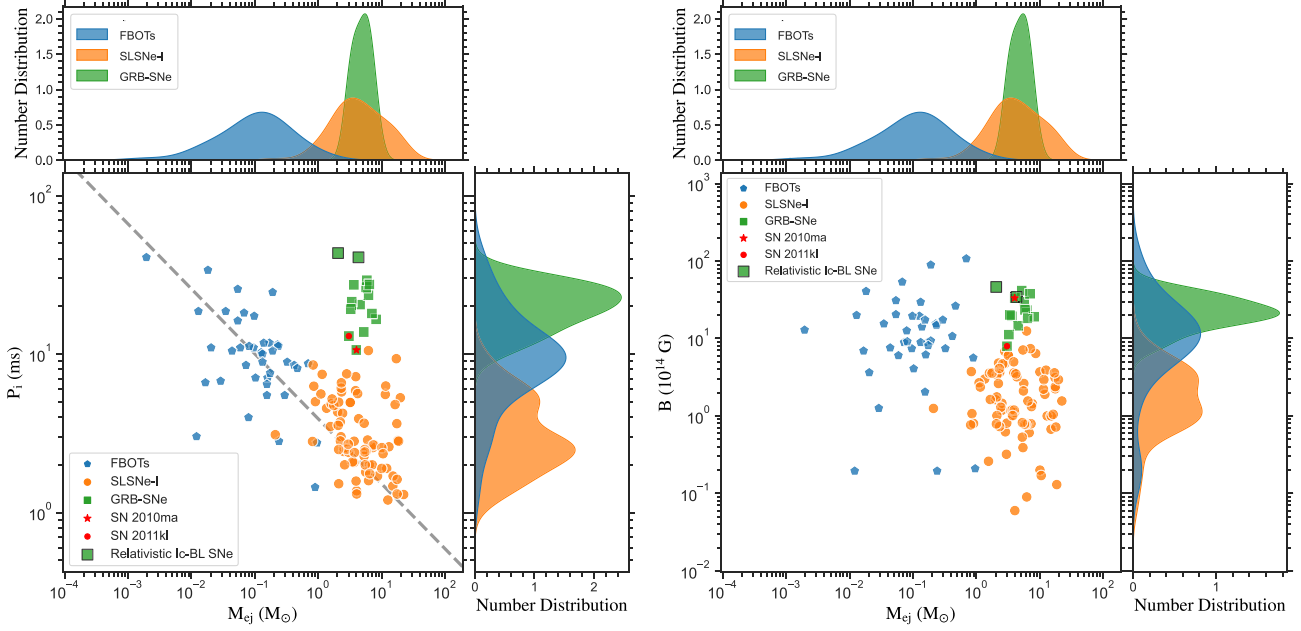
Figure 2. Distribution of GRB-SNe and relativistic Ic-BL SNe in our sample across the parameter space of P_i versus M_{ej} (left-hand panel) and B versus M_{ej} (right-hand panel). SLSNe-I sourced from Yu et al. (2017), Kumar et al. (2021b), and FBOTs taken from Liu et al. (2022) are included on these panels for comparison. The left-hand panel features a grey dashed line illustrating the correlation $P_i \propto M_{ej}^{-0.41}$ from Liu et al. (2022). The top and side plots in both panels provide a normalized number distribution of GRB-SNe, SLSNe-I, and FBOTs for M_{ej}, P_i (left-hand panel), and M_{ej}, B (right-hand panel).

peak luminosities and evolution time-scales and adopting parameters from diverse studies with different light-curve fitting methodologies could be the possible reasons behind comparatively larger parameter dispersion (see Yu et al. 2017; Kumar et al. 2021b and references therein).

None the less, based on the present study, GRB-SNe appear to have M_{ej} values within the range exhibited by SLSNe-I, as also shown in Pandey et al. (2021). Whereas FBOTs seem to hold comparatively lower ejecta masses (see the top sub-panels of Fig. 2). The distribution curves of P_i and B for GRB-SNe peak at higher values than those of SLSNe-I and FBOTs; however, there is a more extensive spread in P_i and B values of FBOTs and cover the full range shown by GRB-SNe. Two relativistic Ic-BL SNe presented in the current study exhibit similar M_{ej}, and higher P_i and B values than those of the entire sample of SLSNe-I and most of the GRB-SNe used in the present study. Furthermore, SN 2010ma and SN 2011kl, the two most luminous GRB-SNe in the present sample, exhibit intermediate P_i values, bridging the gap between GRB-SNe and SLSNe-I. Details about P_i and B parameter distributions among events studied in the present analysis and SLSNe-I, along with LGRBs and SGRBs to understand these critical parameters across a diverse range of cosmic transients, are discussed in the following section.

4.2 Magnetic field versus initial spin period

Here, we discuss the B versus P_i distribution of GRB-SNe and relativistic Ic-BL SNe used in the present study to those of SLSNe-I (Yu et al. 2017; Kumar et al. 2021b), LGRBs (Zou et al. 2019) and SGRBs (Suvorov & Kokkotas 2021; Zou et al. 2021); see Fig. 3.

For LGRBs and SGRBs, Zou et al. (2019) and Suvorov & Kokkotas (2021); Zou et al. (2021), respectively, constrained the values of B and P_i through analysing the early canonical X-ray light curves during the shallow-decaying/plateau phase, potentially resulting from the magnetic dipole radiations emitted by newly born
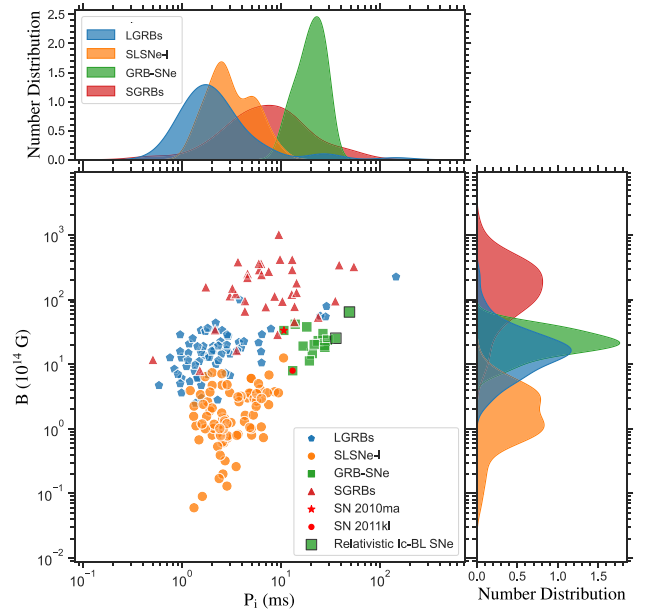

Figure 3. B versus P_i for GRB-SNe and relativistic Ic-BL SNe studied in the present work compared to SLSNe-I, LGRBs, and SGRBs. The right-hand and top subpanels provide a normalized number distribution of GRB-SNe, SLSNe-I, LGRBs, and SGRBs for B and P_i, respectively. All categories of transients discussed here appear to share different B and P_i parameter distributions with some overlapping.

magnetars. Although, Zou et al. (2019, 2021) calculated the B and P_i values considering radiation efficiency (η) of 0.3 therefore we scaled the B and P_i values quoted by Suvorov & Kokkotas (2021) from $\eta = 1$ to 0.3 for consistency. The current analysis, comparing

B versus P_i among GRB-SNe, relativistic Ic-BL SNe, SLSNe-I, LGRBs, and SGRBs, reveals that these events of different classes occupy distinct parameter spaces (see Fig. 3). This emphasizes that magnetars, distinguished by varying *B* and P_i values, can govern different classes of transients. However, we also acknowledge the possibility of sample bias, given that the values are adopted from different references that employ varied methods and assumptions.

The *B* values manifest a noticeable pattern, where SLSNe-I exhibit the lowest, LGRBs intermediate, and SGRBs the highest *B* values (see also Rowlinson et al. 2013; Yi et al. 2014; Yu et al. 2017; Li et al. 2018; Lin et al. 2020; Zou et al. 2021). Nevertheless, there is some observed overlap in their distributions, including a few outliers with values significantly deviating from the sample. Notably, GRB-SNe discussed in this study exhibit *B* values within a similar range to those of LGRBs. On the other hand, the P_i distribution for SLSNe-I, LGRBs, SGRBs, and GRB-SNe also exhibit different parameter spaces but with a higher degree of overlap compared to their *B* counterparts (see the top and left-hand subpanels of Fig. 3). LGRBs tend to have the lowest P_i values, followed by SLSNe-I, SGRBs, and GRB-SNe with the highest P_i values. However, SGRBs demonstrate a broader range of P_i values, with some cases at the higher end overlapping with those of GRB-SNe. The higher *B* and P_i values of SGRBs than those of LGRBs could be attributed to their, respectively, different progenitor systems as collapsing massive stars and compact binary mergers or the dynamical behaviour behind magnetar formation (Hotokezaka et al. 2013; Giacomazzo et al. 2015; Zou et al. 2021). It is also worth mentioning that distribution curves of *B* and P_i for SLSNe-I display dual peaks, potentially corresponding to slow and fast-evolving SLSNe-I, as also suggested by Yu et al. (2017).

GRB-SNe exhibit higher P_i and *B* values than those of SLSNe-I. The P_i is considered as a primary factor governing the jet energy, where lower P_i corresponds to a higher rotation speed of the central engine, which leads to a more energetic jet (Zou et al. 2019; Gottlieb et al. 2023a). Despite comparatively lower P_i than those of GRB-SNe, SLSNe-I still lack GRB-association signatures (except SN 2011kl), which conveys that the jet is unable to bore through the stellar envelope. Thus, the magnetic field appears to play an essential role here; however, the origin of distinct magnetic field values among these transients is still unclear. Nevertheless, one potential reason could be the rotational speed of the progenitor, which could be responsible for both the launch of energetic jets and the source of stronger magnetic fields (Mösta et al. 2015). In the case of SLSNe-I, the weaker magnetic field may lead to the formation of a poorly beamed jet that is unable to bore through the stellar envelope and liberate all of its energy in the ejecta itself, leading to brighter light curves but is unable to form associated GRB (Bucciantini et al. 2009; Senno, Murase & Mészáros 2016; Yu et al. 2017; Zou & Cheng 2018; Shankar et al. 2021). As some of the SLSNe-I share similar *B* and P_i values to those of LGRBs, the possibility of a jet misalignment effect from the line of sight and extended envelope of SLSNe-I, which can dissipate all jet energy still exists. On the other hand, for the two relativistic Ic-BL SNe discussed here, the absence of associated GRBs, despite exceptionally high magnetic field values, may be attributed to a potentially weakened jet energy resulting from their comparatively higher P_i values. For GRB-SNe, where P_i values lie in-between SLSNe-I and relativistic Ic-BL SNe and the magnetic field is relatively stronger, highly beamed and energetic jets could penetrate the stellar envelope, forming the GRB, while a fraction of jet energy is deposited in the ejecta, resulting in relatively lower luminosity than SLSNe-I. In addition, apart from *B* and P_i values, the extent of the stellar envelope, central-engine activity time, and

jet breakout time could be additional factors that govern the amount of energy deposition in the ejecta (Sobacchi et al. 2017; Suzuki & Maeda 2021).

The P_i values comparison among SNe shown in Fig. 3 signifies that magnetars with lower initial spin periods could generate brighter SNe (Uzdensky & MacFadyen 2007). SLSNe-I/two relativistic Ic-BL SNe with lowest/highest P_i values exhibit the highest/lowest luminosities in the present sample, with GRB-SNe displaying medial luminosities and P_i values. The findings discussed above offer a natural explanation for the intermediate luminosity of SN 2011kl (a sole SLSN-I associated with ULGRB and bridging the luminosity gap between SLSNe-I and GRB-SNe) with its intermediate P_i value compared to SLSNe-I and GRB-SNe. This continuum for P_i values of the central engine powering sources among SLSNe-I, SLSN 2011kl/ULGRG, GRB-SNe, and relativistic Ic-BL SNe suggest a pivotal role of P_i in determining the brightness of these events.

4.3 Unsupervised clustering analysis

As discussed in Section 4.1 and depicted in Fig. 2, GRB-SNe, FBOTs, and SLSNe-I reveal distinct occurrences in the P_i versus M_{ej} and *B* versus M_{ej} parameters space with some overlap. However, the identification of precise boundaries proves challenging. This challenge is further exacerbated in the three-dimensional parameter space (M_{ej}, P_i, and *B*), especially as additional parameters become available for a more extensive data set. The surge in data anticipated from large survey programs like the Legacy Survey of Space and Time (LSST; LSST Science Collaboration et al. 2009) amplifies the complexity, rendering manual visual analysis nearly impractical. Consequently, we seek automated and robust solutions for classifying transient phenomena based on their physical parameters (M_{ej}, P_i, and *B* in the present case).

In our scenario, we opt for unsupervised classification due to the limited number of sources (totalling 135; GRB-SNe: 13, SLSNe-I: 82, FBOTs: 40) and the availability of only three parameters (commonly referred to as features in ML terminology) for each source. Traditional supervised classification methods typically demand a more substantial data set for robust model training. The constraint of a small data set (135 samples) and the limited number of parameters (3) prompts us to employ unsupervised classification methods.

Utilizing unsupervised classification models, our objective is to discern whether these models can effectively identify three distinct clusters based on the provided values of M_{ej}, P_i, and *B* and how well the predicted clusters or labels align with the true clusters or labels corresponding to GRB-SNe, SLSNe-I, and FBOTs. The true labels for each set of M_{ej}, P_i, and *B*, indicating whether these correspond to GRB-SNe, SLSNe-I, or FBOTs, are already known. In our context, unsupervised classification models take a 135 × 3 dimensional matrix (135 sources and three parameters) as input and assign one of the three labels (0, 1, or 2) to each set of 1 × 3 parameters as a prediction. The parameters are then plotted as a function of true labels, and the same parameters are overplotted as a function of predicted labels to establish the correspondence between the two sets of labels (SLSNe-I, GRB-SNe, FBOTs, and 0, 1, 2). Following the identification of this correspondence between the true and predicted labels, we calculate the accuracy score of the classification model as the fraction of sources correctly assigned to their true class.

In our preliminary analysis, we employed different unsupervised classification techniques such as *k*-means clustering (MacQueen et al. 1967; Lloyd 1982), Density-Based Spatial Clustering of Applications with Noise (DBSCAN; Ester et al. 1996), and Agglomerative Clustering (Murtagh & Legendre 2014) using
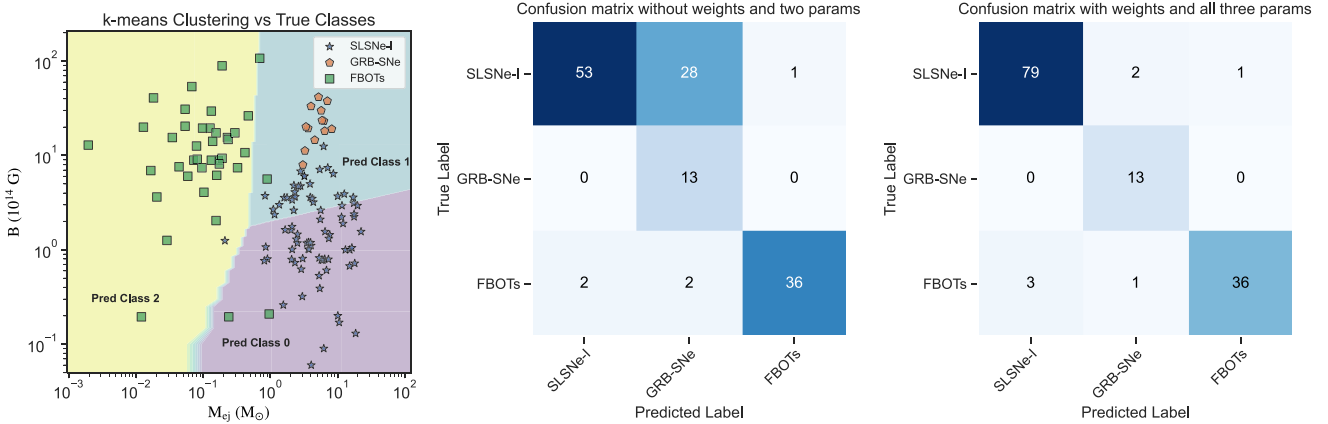
Figure 4. Unsupervised classification of transients employing *k*-means clustering. The left-hand panel depicts the distribution of true classes and their respective mapping to the predicted classes (Class 0, 1, and 2), showcasing the decision boundaries for the three predicted classes as shaded regions. SLSNe-I, FBOTs, and GRB-SNe are mapped to classes 0, 1, and 2, respectively. The middle and right-hand panels present the performance assessment of unsupervised classification through the confusion matrix. In the middle panel, the confusion matrix is derived without assigning weights to samples and utilizing only parameters $M_{\rm ej}$ and B. In the right-hand panel, the confusion matrix is obtained by considering all three parameters ($M_{\rm ej}$, $P_{\rm i}$, and B) and incorporating weights for each sample. Please note that the mapping corresponding to the confusion matrix in the right-hand panel is not presented, as it is challenging to represent or distinguish the transients in a three-dimensional space.

Table 2. Performance comparison of various unsupervised clustering methods adopted for the preliminary analysis (using parameters $M_{\rm ej}$ and B). Accuracy scores are computed using the predictive mapping approach, as discussed in Section 4.3.

Method	Average accuracy (per cent)
k-means	76
DBSCAN	59
Agglomerative clustering	58

PYTHONscikit-learn package (Pedregosa et al. 2011)[3] for the parameters $M_{\rm ej}$ and B to determine their comparative performance, using the accuracy score. The left-hand panel of Fig. 4 illustrates the *k*-means clustering analysis, where the predicted classes 0, 1, and 2 correspond to SLSNe-I, GRB-SNe, and FBOTs, respectively. Based on this predictive mapping, we construct a confusion matrix (see the middle panel of Fig. 4) to quantify the agreement between predicted and true labels and subsequently estimate the accuracy score. Our findings indicate that *k*-means clustering achieves the highest accuracy, registering at 76 per cent, surpassing the performance of other employed unsupervised classification algorithms (see Table 2). Following the observed performances, we decide to proceed with the *k*-means clustering method for all subsequent analyses.

We notice that around 34 per cent (28 out of 82) of the SLSNe-I wrongly fall in the region occupied by the GRB-SNe by *k*-means clustering (middle panel of Fig. 4), which suggests that the decision boundary between these two classes has not been correctly identified. Furthermore, when incorporating all three parameters ($M_{\rm ej}$, $P_{\rm i}$, and B), there is a marginal increase in the accuracy score to 77 per cent. We observe a notable imbalance in the data set, particularly in the smaller sample size of GRB-SNe compared to the other two classes. To rectify this imbalance, we adopt a weighted approach during clustering, assigning greater importance to under-represented classes. We introduce weights based on class counts, with the class exhibiting the maximum count (SLSNe-I) receiving a weight of 1.

The weights for the other classes are determined proportionally to their counts relative to the maximum count (FBOTs: 2.05, GRB-SNe: 6.31). By incorporating weights into the analysis and considering all three parameters, we achieved an accuracy score of 95 per cent. The confusion matrix is presented in the right-hand panel of Fig. 4.

On the other hand, for the sample of SLSNe-I, LGRBs, and SGRBs discussed in Section 4.2, the available parameters are limited to $P_{\rm i}$ and B only. Including the GRB-SNe sample from this study, we repeat unsupervised clustering analysis solely based on $P_{\rm i}$ and B, resulting in an accuracy of 83.5 per cent. The transient classes, SLSNe-I, SGRBs, LGRBs, and GRB-SNe, are mapped to predicted classes 0, 1, 2, and 3, respectively, as illustrated in the left-hand panel of Fig. 5. The corresponding confusion matrix is presented in the right-hand panel of Fig. 5.

Besides average accuracy, precision, recall, and F1-score are essential parameters that assess the performance of a classification model. Precision measures the proportion of correctly classified instances within a particular class out of all instances assigned to that class. Recall, on the other hand, quantifies the fraction of actual instances belonging to a specific class that the model correctly identifies. These two metrics are combined to compute the F1-score, defined by the following equations:

$$\text{Precision} = \frac{\text{Correctly classified instances in a class}}{\text{Total classified instances in that class}},$$

$$\text{Recall} = \frac{\text{Correctly classified instances in a class}}{\text{Total instances in that class}},$$

$$F1 = 2 \times \frac{\text{Precision} \times \text{Recall}}{\text{Precision} + \text{Recall}}.$$

The summary of the classifications performed using *k*-means clustering in terms of the above-described metrics is reported in Table 3. In the clustering analysis, we initially employed an unsupervised machine learning approach, specifically *k*-means clustering, to classify transients based on photometrically derived parameters from the light curves. This approach yielded a respectable accuracy of 77 per cent for the three parameters ($M_{\rm ej}$, $P_{\rm i}$, and B). However, it is important to note that the introduction of weights in the clustering algorithm renders the approach semisupervised rather than
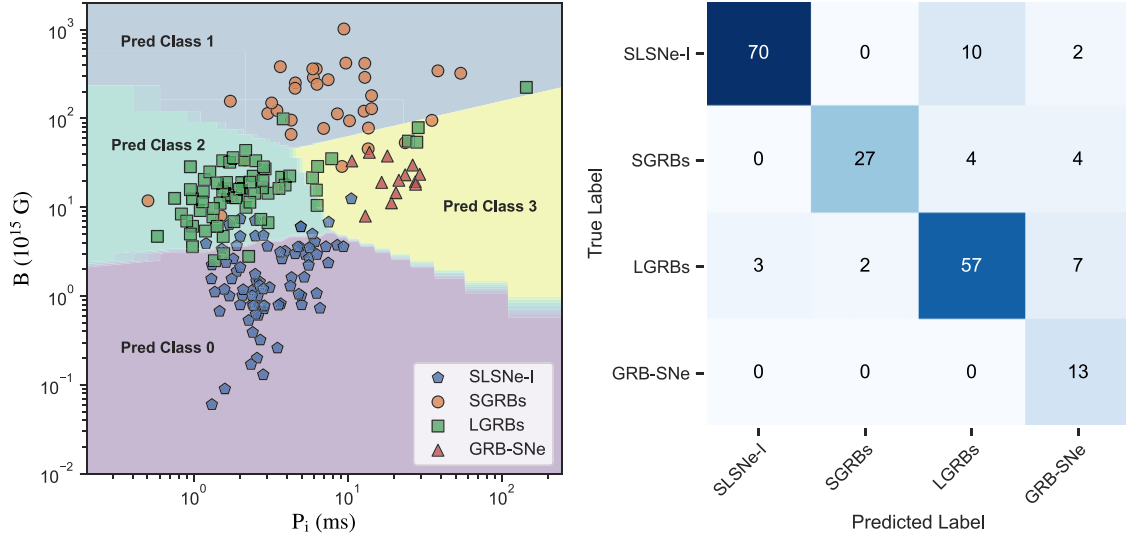
Figure 5. Left-hand panel: unsupervized classification of LGRBs, SGRBs, SLSNe-I, and GRB-SNe sample and their mapping to the predicted classes (Class 0, 1, 2, and 3). Right-hand panel: confusion matrix for the unsupervized classification of LGRBs, SGRBs, SLSNe-I, and GRB-SNe sample.

Table 3. Performance metrics for classifications examined in this study using *k*-means clustering.

Experiment	Class	Precision	Recall	F1-score	No. of sources
Without weights and two parameters	SLSNe-I	0.96	0.65	0.77	82
(M_{ej} and B)	GRB-SNe	0.30	1.00	0.46	13
	FBOTs	0.97	0.90	0.94	40
	Average accuracy: 76 per cent				135
	SLSNe-I	0.96	0.96	0.96	82
With weights and three parameters	GRB-SNe	0.81	1.00	0.90	13
(M_{ej}, P_i, and B)	FBOTs	0.97	0.90	0.94	40
	Average accuracy: 95 per cent				135
Classification of LGRBs, SGRBs,	SLSNe-I	0.96	0.85	0.90	82
SLSNe-I, and GRB-SNe sample	SGRBs	0.93	0.77	0.84	35
based on P_i and B	LGRBs	0.80	0.83	0.81	69
	GRB-SNe	0.50	1.00	0.67	13
	Average accuracy: 84 per cent				199

fully unsupervised. This transition occurs as the algorithm begins to incorporate additional information, such as prior knowledge or domain expertise, to guide the clustering process.

5 CONCLUSION

In this paper, we present the semi-analytical light curve modelling of a sample of 13 GRB-SNe with adequate data in the literature, along with two relativistic and central-engine-driven Ic-BL SNe 2009bb and 2012ap. The light curve modelling is performed under the MAG model and employing the MINIM code, considering these events are primarily powered by centrally-located spin-down millisecond magnetars. The MAG model well regenerated the light curves of all 15 events in our sample with χ^2/dof close to one. The M_{ej} and V_{exp} values for all the events in our sample constrained through MINIM light curve modelling are consistent with those quoted in the literature, except SN 2010ma, which exhibits an offset in M_{ej} value.

GRB-SNe exhibit key parameters with median values, $E_p \approx 4.8 \times 10^{49}$ erg, $t_d \approx 17$ d, $t_p \approx 5.4$ d, $R_p \approx 7.2 \times 10^{13}$ cm, $V_{exp} \approx 24\,000$ km s^{-1}, $M_{ej} \approx 5.2\,M_\odot$, $P_i \approx 20.5$ ms, and $B \approx 20.1 \times 10^{14}$ G. Within our sample, SN 2011kl and SN 2010ma, the two brightest

events, exhibit the lowest P_i values, whereas SN 2011kl also shows the lowest B value. On the other hand, the relativistic Ic-BL SNe 2009bb and SN 2012ap share the highest P_i and B values than those of GRB-SNe (except SN 2006aj) presented in the current study.

The M_{ej}, P_i, and B parameters comparison among GRB-SNe, two relativistic Ic-BL SNe, SLSNe-I, and FBOTs do not show any noteworthy correlation among P_i and M_{ej} or B and M_{ej}. None the less, GRB-SNe and relativistic Ic-BL SNe presented here hold a different parameter space in P_i versus M_{ej} and B versus M_{ej} distributions. GRB-SNe appear to have closer M_{ej} values than most of the SLSNe-I; however, they share higher M_{ej} values than those of FBOTs. The two relativistic Ic-BL SNe 2009bb and SN 2012ap show comparable M_{ej} and higher P_i and B values than those of the entire sample of SLSNe-I and most of the GRB-SNe used in the present study, which further suggests a different nature of the central engines among these events.

Furthermore, P_i versus B distribution of GRB-SNe and two relativistic Ic-BL SNe presented here also retain a different parameter space than those of SLSNe-I, LGRBs, and SGRBs, while there is a small degree of overlapping exists. SLSNe-I, LGRBs, and SGRBs display an ascending trend in B values corresponding to the peak

of the distribution curves, with GRB-SNe having B values closer to those of LGRBs. On the other hand, within the P_i parameter space, a discernible ascending order exists among LGRBs, SLSNe-I, SGRBs, and GRB-SNe.

Besides this, in the P_i versus B distribution, SGRBs demonstrate higher B and P_i values compared to LGRBs, which indicate the diverse behaviour of the magnetars originating from the different progenitor systems related to these events. For SLSNe-I, both B and P_i distribution curves show bimodal distributions, possibly pertaining to two subclasses (slow and fast-evolving) of SLSNe-I. This analysis indicates a possible continuum in P_i versus B parameters space among SLSNe-I, SN 2011kl (faintest SLSN but brightest GRB-SN), GRB-SNe, and two relativistic Ic-BL SNe, highlighting their crucial role in governing the luminosity of these events. This study also motivates us to perform light curve modelling on different classes of SNe in the literature, from lower luminosity events to SLSNe, under a single model to look for a continuum among the parameters of their underlying powering sources.

In a novel exploration, we employ machine-learning techniques to investigate the distinctiveness of the physical parameters of the discussed transients. The application of the k-means clustering algorithm to the parameters P_i, B, and M_{ej} for GRB-SNe, FBOTs, and SLSNe-I yields an accuracy of 95 per cent, indicating clear separation in parameter space. Extending this analysis to classify GRB-SNe, SLSNe-I, LGRBs, and SGRBs within the available parameters space of P_i and B results in an accuracy of approximately 84 per cent. These findings underscore the significance of employing machine learning algorithms, particularly with larger data sets facilitated by all-sky surveys, to analyse and interpret the multidimensional parameter space proficiently. As a future scope of this work, we intend to compile a more extensive data set of these extragalactic cosmic explosions from the literature and leverage advancements in machine learning for transient astronomy.

ACKNOWLEDGEMENTS

DATA AVAILABILITY

Data can be shared upon request to the corresponding author.

REFERENCES

Abbott B. P. et al., 2017a, ApJ, 848, L12
Abbott B. P. et al., 2017b, ApJ, 848, L13
Aguilera-Dena D. R., Langer N., Moriya T. J., Schootemeijer A., 2018, ApJ, 858, 115
Ahumada T. et al., 2021, Nat. Astron., 5, 917
Aimuratov Y. et al., 2023, ApJ, 955, 93
Angus C. R., Levan A. J., Perley D. A., Tanvir N. R., Lyman J. D., Stanway E. R., Fruchter A. S., 2016, MNRAS, 458, 84
Arnett W. D., 1982, ApJ, 253, 785
Arnett W. D., Fu A., 1989, ApJ, 340, 396
Ashall C. et al., 2019, MNRAS, 487, 5824
Barnes J., Duffell P. C., Liu Y., Modjaz M., Bianco F. B., Kasen D., MacFadyen A. I., 2018, ApJ, 860, 38
Becerra R. L. et al., 2017, ApJ, 837, 116
Bernardini M. G., 2015, JHEA, 7, 64
Bietenholz M. F. et al., 2010, ApJ, 725, 4
Boone K., 2019, AJ, 158, 257
Brachetti P. e. a., 1997, J. Glob. Optim., 10, 10
Bucciantini N., Quataert E., Arons J., Metzger B. D., Thompson T. A., 2008, MNRAS, 383, L25
Bucciantini N., Quataert E., Metzger B. D., Thompson T. A., Arons J., Del Zanna L., 2009, MNRAS, 396, 2038
Bufano F. et al., 2012, ApJ, 753, 67
Burlon D., Ghirlanda G., Ghisellini G., Lazzati D., Nava L., Nardini M., Celotti A., 2008, ApJ, 685, L19
Burrows A., Vartanyan D., 2021, Nature, 589, 29
Cano Z. et al., 2011, ApJ, 740, 41
Cano Z. et al., 2015, MNRAS, 452, 1535
Cano Z. et al., 2017a, A&A, 605, A107
Cano Z., Johansson Andreas K. G., Maeda K., 2016, MNRAS, 457, 2761
Cano Z., Wang S.-Q., Dai Z.-G., Wu X.-F., 2017b, Adv. Astron., 2017, 8929054
Chakraborti S. et al., 2015, ApJ, 805, 187
Chatzopoulos E., Tuminello R., 2019, ApJ, 874, 68
Chatzopoulos E., Wheeler J. C., Vinko J., 2012, ApJ, 746, 121
Chatzopoulos E., Wheeler J. C., Vinko J., Horvath Z. L., Nagy A., 2013, ApJ, 773, 76
Chen J.-M., Zhu K.-R., Peng Z.-Y., Zhang L., 2023, MNRAS, 527, 4272
Chornock R. et al., 2010, preprint (arXiv:1004.2262)
D'Elia V. et al., 2015, A&A, 577, A116
Dai C.-Y., Guo C.-L., Zhang H.-M., Liu R.-Y., Wang X.-Y., 2024, ApJ, 962L, 37D
Dai Z. G., Lu T., 1998, A&A, 333, L87
Dai Z. G., Wang X. Y., Wu X. F., Zhang B., 2006, Science, 311, 1127
Dainotti M. G., De Simone B., Islam K. M., Kawaguchi K., Moriya T. J., Takiwaki T., Tominaga N., Gangopadhyay A., 2022, ApJ, 938, 41
Dall'Osso S., Perna R., Tanaka T. L., Margutti R., 2017, MNRAS, 464, 4399
de Soto K. M. et al., 2024, preprint (arXiv:2403.07975)
de Ugarte Postigo A. et al., 2017, GRB Coordinates Network, 22096, 1
Deng J., Tominaga N., Mazzali P. A., Maeda K., Nomoto K., 2005, ApJ, 624, 898
Dessart L., 2019, A&A, 621, A141
Dessart L., Hillier D. J., Waldman R., Livne E., Blondin S., 2012, MNRAS, 426, L76
Dimple, Misra, K., Arun K. G., 2023, ApJ, 949, L22
Drout M. R. et al., 2014, ApJ, 794, 23
Duncan R. C., Thompson C., 1992, ApJ, 392, L9
Eichler D., Livio M., Piran T., Schramm D. N., 1989, Nature, 340, 126
Ester M., Kriegel H.-P., Sander J., Xu X., 1996, in A Density-Based Algorithm for Discovering Clusters in Large Spatial Data-bases with Noise. Proceedings of 2nd International Conference on Knowledge Discovery and Data Mining (KDD), Portland, Oregon, AAAI Press, p.226
Fang K., Metzger B. D., Murase K., Bartos I., Kotera K., 2019, ApJ, 878, 34
Fox D. B., Mészáros P., 2006, NJP, 8, 199
Fulton M. D. et al., 2023, ApJ, 946, L22
Galama T. J. et al., 1998, Nature, 395, 670
Ghirlanda G., Bosnjak Z., Ghisellini G., Tavecchio F., Firmani C., 2007, MNRAS, 379, 73

Giacomazzo B., Zrake J., Duffell P. C., MacFadyen A. I., Perna R., 2015, ApJ, 809, 39

Gibson S. L., Wynn G. A., Gompertz B. P., O'Brien P. T., 2017, MNRAS, 470, 4925

Gibson S. L., Wynn G. A., Gompertz B. P., O'Brien P. T., 2018, MNRAS, 478, 4323

Gillanders J. H. et al., 2023, preprint (arXiv:2308.00633)

Goldstein A. et al., 2017, ApJ, 848, L14

Gompertz B. P. et al., 2023, Nat. Astron., 7, 67

Gompertz B. P., O'Brien P. T., Wynn G. A., 2014, MNRAS, 438, 240

Gompertz B. P., O'Brien P. T., Wynn G. A., Rowlinson A., 2013, MNRAS, 431, 1745

Gompertz B. P., van der Horst A. J., O'Brien P. T., Wynn G. A., Wiersema K., 2015, MNRAS, 448, 629

Gompertz B., Fruchter A., 2017, ApJ, 839, 49

Gottlieb O. et al., 2023b, ApJ, 958, L33

Gottlieb O., Jacquemin-Ide J., Lowell B., Tchekhovskoy A., Ramirez-Ruiz E., 2023a, ApJ, 952, L32

Greiner J. et al., 2015, Nature, 523, 189

Gutiérrez C. P. et al., 2021, MNRAS, 504, 4907

Ho A. Y. Q. et al., 2023, Nature, 623, 927

Hotokezaka K., Kashiyama K., Murase K., 2017, ApJ, 850, 18

Hotokezaka K., Kiuchi K., Kyutoku K., Okawa H., Sekiguchi Y.-i., Shibata M., Taniguchi K., 2013, Phys. Rev. D, 87, 024001

Hu R.-C. et al., 2023, preprint (arXiv:2301.06402)

Inserra C. et al., 2013, ApJ, 770, 128

Inserra C., 2019, Nat. Astron., 3, 697

Iwamoto K. et al., 1998, Nature, 395, 672

Izzo L. et al., 2019, Nature, 565, 324

Kann D. A. et al., 2019, A&A, 624, A143

Kasen D., Bildsten L., 2010, ApJ, 717, 245

Kashiyama K., Murase K., Bartos I., Kiuchi K., Margutti R., 2016, ApJ, 818, 94

Kelly P. L., Kirshner R. P., Pahre M., 2008, ApJ, 687, 1201

Kisley M., Qin Y.-J., Zabludoff A., Barnard K., Ko C.-L., 2023, ApJ, 942, 29

Klose S. et al., 2019, A&A, 622, A138

Kouveliotou C., Meegan C. A., Fishman G. J., Bhat N. P., Briggs M. S., Koshut T. M., Paciesas W. S., Pendleton G. N., 1993, ApJ, 413, L101

Kumar A. et al., 2020, ApJ, 892, 28

Kumar A. et al., 2021b, MNRAS, 502, 1678

Kumar A., Pandey S. B., Gupta R., Aryan A., Castro-Tirado A. J., Brahme N., 2021a, in Revista Mexicana de Astronomia y Astrofisica Conference Series, Vol. 53. VI Workshop on Robotic Autonomous Observatories, Huelva, Spain, p. 127

Kumar A., Pandey S. B., Gupta R., Aryan A., Ror A. K., Sharma S., Brahme N., 2022, New A, 97, 101889

Kumar P., Zhang B., 2015, Phys. Rep., 561, 1

Levan A. et al., 2024, Nature, 626, 737

Levan A., Crowther P., de Grijs R., Langer N., Xu D., Yoon S.-C., 2016, Space Sci. Rev., 202, 33

Levesque E. M. et al., 2010, ApJ, 709, L26

Li L., Wu X.-F., Lei W.-H., Dai Z.-G., Liang E.-W., Ryde F., 2018, ApJS, 236, 26

Li Q. M., Zhang Z. B., Han X. L., Zhang K. J., Xia X. L., Hao C. T., 2023, MNRAS, 524, 1096

Li X., Hjorth J., 2014, preprint (arXiv:1407.3506)

Lian J.-S., Wang S.-Q., Gan W.-P., Li J.-Y., Liang E.-W., 2022, ApJ, 931, 90

Lin W. L., Wang X. F., Wang L. J., Dai Z. G., 2020, ApJ, 903, L24

Liu J.-F., Zhu J.-P., Liu L.-D., Yu Y.-W., Zhang B., 2022, ApJ, 935, L34

Liu Z., Zhao X.-L., Huang F., Wang X.-F., Zhang T.-M., Chen J.-C., Zhang T.-J., 2015, Res. Astron. Astrophys., 15, 225

Lloyd S., 1982, IEEE Trans. Inf. Theory, 28, 129

LSST Science Collaboration et al., 2009, preprint (arXiv:0912.0201)

Lü H.-J., Lan L., Zhang B., Liang E.-W., Kann D. A., Du S.-S., Shen J., 2018, ApJ, 862, 130

Lü H.-J., Zhang B., Lei W.-H., Li Y., Lasky P. D., 2015, ApJ, 805, 89

Lunnan R. et al., 2014, ApJ, 787, 138

Lunnan R. et al., 2015, ApJ, 804, 90

Lyons N., O'Brien P. T., Zhang B., Willingale R., Troja E., Starling R. L. C., 2010, MNRAS, 402, 705

MacQueen J. et al., 1967, Proceedings of the fifth Berkeley symposium on mathematical statistics and probability, Vol. 1. Some methods for classification and analysis of multivariate observations, University of California Press, Oakland, CA, USA, p. 281

Maeda K. et al., 2007, ApJ, 666, 1069

Maeder A., Meynet G., 2012, Rev. Mod. Phys., 84, 25

Margalit B., Metzger B. D., Berger E., Nicholl M., Eftekhari T., Margutti R., 2018, MNRAS, 481, 2407

Margutti R. et al., 2013, ApJ, 778, 18

Margutti R. et al., 2014, ApJ, 797, 107

Mazzali P. A. et al., 2003, ApJ, 599, L95

Mazzali P. A. et al., 2006a, Nature, 442, 1018

Mazzali P. A. et al., 2006b, ApJ, 645, 1323

Mazzali P. A., McFadyen A. I., Woosley S. E., Pian E., Tanaka M., 2014, MNRAS, 443, 67

Melandri A. et al., 2012, A&A, 547, A82

Melandri A. et al., 2014, A&A, 567, A29

Melandri A. et al., 2019, MNRAS, 490, 5366

Melandri A. et al., 2022, A&A, 659, A39

Meszaros P., Rees M. J., 1993, ApJ, 405, 278

Metzger B. D., 2019, Living Rev. Relativ., 23, 1

Metzger B. D., Giannios D., Thompson T. A., Bucciantini N., Quataert E., 2011, MNRAS, 413, 2031

Metzger B. D., Margalit B., Kasen D., Quataert E., 2015, MNRAS, 454, 3311

Milisavljevic D. et al., 2015, ApJ, 799, 51

Modjaz M., Liu Y. Q., Bianco F. B., Graur O., 2016, ApJ, 832, 108

Mösta P., Ott C. D., Radice D., Roberts L. F., Schnetter E., Haas R., 2015, Nature, 528, 376

Murtagh F., Legendre P., 2014, J. Classif., 31, 274

Nagy A. P., 2018, ApJ, 862, 143

Narayan R., Piran T., Kumar P., 2001, ApJ, 557, 949

Nicholl M., 2018, Res. Notes Am. Astron. Soc., 2, 230

Nicholl M., Berger E., Margutti R., Blanchard P. K., Milisavljevic D., Challis P., Metzger B. D., Chornock R., 2017, ApJ, 835, L8

Olivares E. F. et al., 2012, A&A, 539, A76

Olivares E. F. et al., 2015, A&A, 577, A44

Omand C. M. B., Jerkstrand A., 2023, A&A, 673, A107

Omand C. M. B., Sarin N., 2024, MNRAS, 527, 6455

Ostriker J. P., Gunn J. E., 1971, ApJ, 164, L95

Pandey S. B. et al., 2021, MNRAS, 507, 1229

Patat F. et al., 2001, ApJ, 555, 900

Pedregosa F. et al., 2011, JMLR, 12, 2825

Perley D. A. et al., 2019, MNRAS, 484, 1031

Pian E. et al., 2006, Nature, 442, 1011

Pian E. et al., 2017, Nature, 551, 67

Pignata G. et al., 2011, ApJ, 728, 14

Piran T., 1999, Phys. Rep., 314, 575

Piran T., 2004, Rev. Mod. Phys., 76, 1143

Popham R., Woosley S. E., Fryer C., 1999, ApJ, 518, 356

Prentice S. J. et al., 2018, ApJ, 865, L3

Pursiainen M. et al., 2018, MNRAS, 481, 894

Quimby R. M. et al., 2011, Nature, 474, 487

Rastinejad J. C. et al., 2022, Nature, 612, 223

Rossi A. et al., 2022, ApJ, 932, 1

Rowlinson A. et al., 2010, MNRAS, 409, 531

Rowlinson A., Gompertz B. P., Dainotti M., O'Brien P. T., Wijers R. A. M. J., van der Horst A. J., 2014, MNRAS, 443, 1779

Rowlinson A., O'Brien P. T., Metzger B. D., Tanvir N. R., Levan A. J., 2013, MNRAS, 430, 1061

Saji J., Iyyani S., Mazde K., 2023, ApJS, 269, 2

Schlafly E. F., Finkbeiner D. P., 2011, ApJ, 737, 103

Schulze S. et al., 2014, A&A, 566, A102

Senno N., Murase K., Mészáros P., 2016, Phys. Rev. D, 93, 083003

Shankar S., Mösta P., Barnes J., Duffell P. C., Kasen D., 2021, MNRAS, 508, 5390

Sharma K. et al., 2020b, MNRAS, 496, 5002

Sharma K., Kembhavi A., Kembhavi A., Sivarani T., Abraham S., Vaghmare K., 2020a, MNRAS, 491, 2280

Sobacchi E., Granot J., Bromberg O., Sormani M. C., 2017, MNRAS, 472, 616

Soderberg A. M. et al., 2006, Nature, 442, 1014

Sun H. et al., 2023, preprint (arXiv:2307.05689)

Suvorov A. G., Kokkotas K. D., 2021, MNRAS, 502, 2482

Suzuki A., Maeda K., 2021, ApJ, 908, 217

Suzuki A., Maeda K., Shigeyama T., 2019, ApJ, 870, 38

Tanaka M., 2016, Adv. Astron., 2016, 634197

Thompson C., 1994, MNRAS, 270, 480

Toy V. L. et al., 2016, ApJ, 818, 79

Troja E. et al., 2007, ApJ, 665, 599

Troja E. et al., 2017, Nature, 551, 71

Troja E. et al., 2022, Nature, 612, 228

Troja E., Rosswog S., Gehrels N., 2010, ApJ, 723, 1711

Usov V. V., 1992, Nature, 357, 472

Uzdensky D. A., MacFadyen A. I., 2007, ApJ, 669, 546

Valenti S. et al., 2017, ApJ, 848, L24

Villar V. A. et al., 2020, ApJ, 905, 94

Wang H. et al., 2017b, ApJ, 851, L18

Wang J. et al., 2018, ApJ, 867, 147

Wang L. J. et al., 2017a, ApJ, 837, 128

Wang L.-J., Han Y.-H., Xu D., Wang S.-Q., Dai Z.-G., Wu X.-F., Wei J.-Y., 2016, ApJ, 831, 41

Wang L., Wheeler J. C., 1998, ApJ, 504, L87

Wheeler J. C., Johnson V., Clocchiatti A., 2015, MNRAS, 450, 1295

Wheeler J. C., Yi I., Höflich P., Wang L., 2000, ApJ, 537, 810

Woosley S. E., 1993, ApJ, 405, 273

Woosley S. E., 2010, ApJ, 719, L204

Woosley S. E., Bloom J. S., 2006, ARA&A, 44, 507

Woosley S. E., Heger A., Weaver T. A., 2002, Rev. Mod. Phys., 74, 1015

Yang J. et al., 2022, Nature, 612, 232

Yi S. X., Dai Z. G., Wu X. F., Wang F. Y., 2014, preprint (arXiv:1401.1601)

Yu Y.-W., Zhu J.-P., Li S.-Z., Lü H.-J., Zou Y.-C., 2017, ApJ, 840, 12

Zhang B. B. et al., 2021, Nat. Astron., 5, 911

Zhang B., 2019, The physics of gamma-ray bursts. Cambridge University Press, Cambridge CambridgeISBN:1-108-67683-9

Zhang B., Mészáros P., 2001, ApJ, 552, L35

Zhang W., Woosley S. E., Heger A., 2004, ApJ, 608, 365

Zhang Z.-D., Yu Y.-W., Liu L.-D., 2022, ApJ, 936, 54

Zou L. et al., 2021, MNRAS, 508, 2505

Zou L., Zhou Z.-M., Xie L., Zhang L.-L., Lü H.-J., Zhong S.-Q., Wang Z.-J., Liang E.-W., 2019, ApJ, 877, 153

Zou Y.-C., Cheng K. S., 2018, PASA, 35, e032

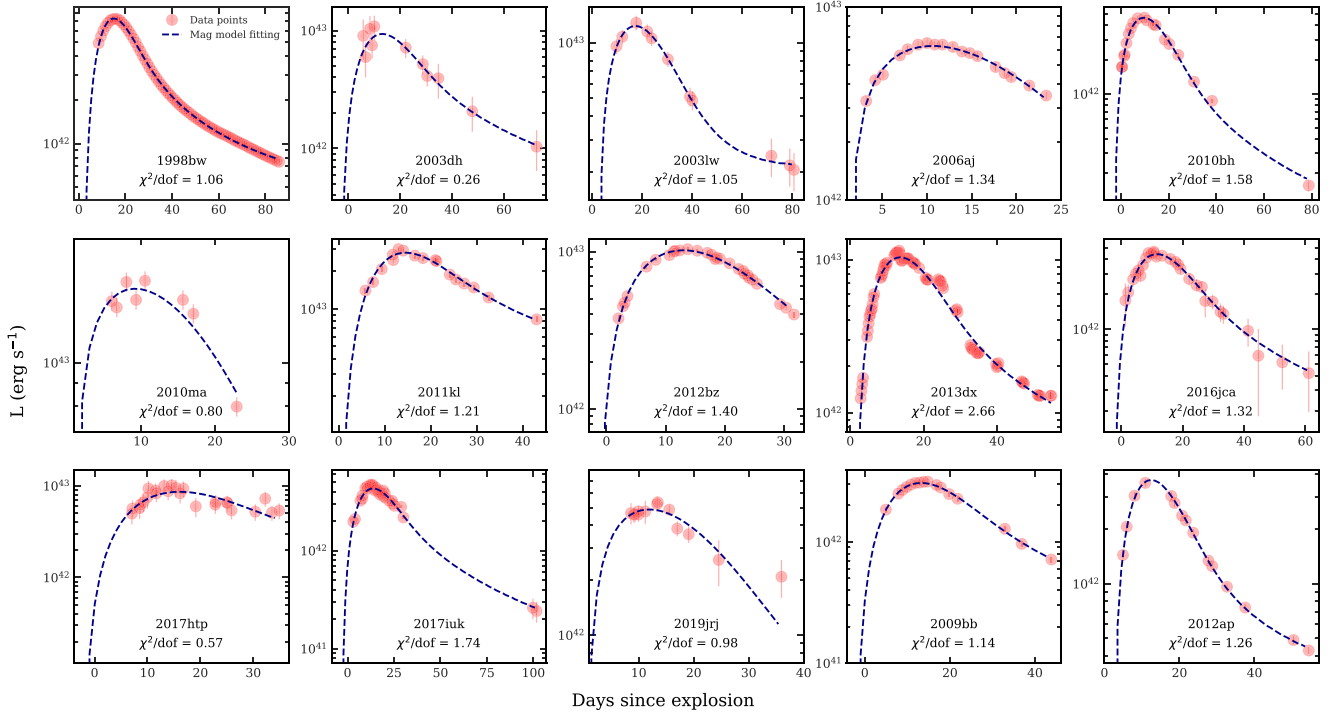# APPENDIX A: MINIM LIGHT CURVE FITTING RESULTS

Figure A1. Semi-analytical light-curve modelling results of 13 GRB-SNe and two relativistic central-engine-driven Ic-BL SNe, employing the MAG model within the MINIM code (Chatzopoulos et al. 2013), are shown. The pseudo-bolometric light curves of all 15 SNe in the current sample are reproduced with low χ^2/dof values, and the estimated parameters are tabulated in Table 1.
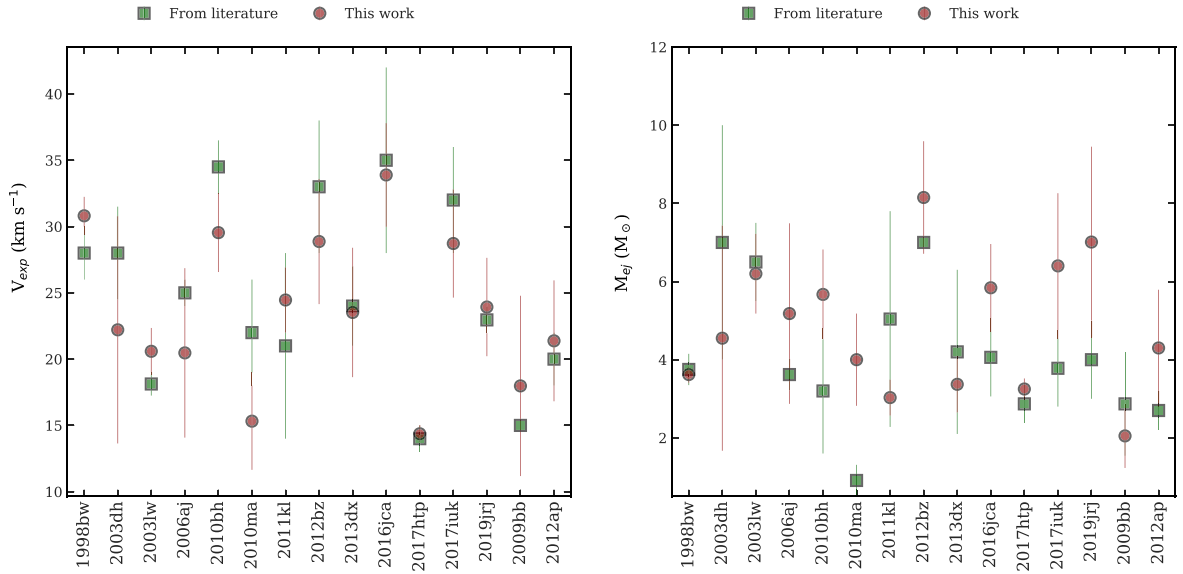

Figure A2. V_{exp} and M_{ej} comparison between the values estimated in the present study and those taken from the literature for a sample of 15 SNe used here: 1998bw (Iwamoto et al. 1998; Patat et al. 2001; Cano et al. 2011); 2003dh (Mazzali et al. 2003; Deng et al. 2005; Modjaz et al. 2016), 2003lw (Mazzali et al. 2006b), 2006aj (Pian et al. 2006; Mazzali et al. 2006a; Zhang, Yu & Liu 2022), 2010bh (Chornock et al. 2010; Cano et al. 2011; Bufano et al. 2012; Olivares E. et al. 2012), 2010ma (Olivares E. et al. 2015), 2011kl (Greiner et al. 2015; Kann et al. 2019), 2012bz (Melandri et al. 2012; Schulze et al. 2014), 2013dx (D'Elia et al. 2015; Toy et al. 2016), 2016jca (Cano et al. 2017a; Ashall et al. 2019), 2017htp (Melandri et al. 2019), 2017iuk (Izzo et al. 2019), SN 2019jrj (Melandri et al. 2022), 2009bb (Pignata et al. 2011), and 2012ap (Liu et al. 2015; Milisavljevic et al. 2015). The M_{ej} and V_{exp} values constrained through MINIM light curve modelling in the present study and those taken from the literature are consistent for all the events in our sample (except M_{ej} value for SN 2010ma).

This paper has been typeset from a TeX/LaTeX file prepared by the author.